Mapping Octahedral Tilts and Polarization Across a Domain Wall in $BiFeO_3$ from Z-Contrast Scanning Transmission Electron Microscopy Image Atomic Column Shape Analysis

AlbinaY. Borisevich,[†,*] Oleg S. Ovchinnikov,[‡] Hye Jung Chang,[†] Mark P. Oxley,[†,§] Pu Yu,[⊥] Jan Seidel,[⊥] Eugine A. Eliseev,[∥] Anna N. Morozovska,[#] Ramamoorthy Ramesh,[⊥] Stephen J. Pennycook,[†] and Sergei V. Kalinin[†]

[†]Oak Ridge National Laboratory, Oak Ridge, Tennessee 37831, United States, [‡]Department of Physics and Astronomy, University of Tennessee, Knoxville, Tennessee 37996, United States, [§]Department of Physics, Vanderbilt University, Nashville, Tennessee, 37240 United States, [⊥]Department of Materials Science and Engineering, University of California, Berkeley, California, 94720 United States, and [∥]Institute for Problems of Materials Science and [#]Institute of Semiconductor Physics, National Academy of Sciences of Ukraine, Kiev, Ukraine

ABSTRACT Oxygen octahedral tilts underpin the functionality of a large number of perovskite-based materials and heterostructures with competing order parameters. We show how a precise analysis of atomic column shapes in Z-contrast scanning transmission electron microscopy images can reveal polarization and octahedral tilt behavior across uncharged and charged domain walls in $BiFeO_3$. This method is capable of visualizing octahedral tilts to much higher thicknesses than phase contrast imaging. We find that the octahedral tilt transition across a charged domain wall is atomically abrupt, while the associated polarization profile is diffuse (1.5−2 nm). Ginzburg−Landau theory then allows the relative contributions of polarization and the structural order parameters to the wall energy to be determined.

KEYWORDS: ferroelectric domain walls · bismuth ferrite · scanning transmission electron microscopy · principal component analysis.

The multifaceted magnetic, electrical, and structural functionalities of perovskite ABO_3 materials are underpinned by the subtle distortions of the crystallographic lattice from the prototype cubic phase.[1] These distortions include relative displacements of the cations from the centers of the BO_6 oxygen octahedra, deformations of the oxygen octahedra, and collective tilts of the octahedral network. In ferroelectrics, the condensation of zone center soft phonon modes gives rise to the shift of the B-site cation from the octahedral center and to the emergence of spontaneous polarization and associated tetragonal lattice distortion.[2] The zone-boundary modes lead to a broad range of structural instabilities, intimately related to magnetic and metal−insulator transitions in distorted perovskites. The deformations of oxygen octahedra driven by collective Jahn−Teller distortions control both metal−insulator transitions and magnetic properties.[3] Finally, octahedral tilts driven by steric interactions define the symmetry group of the material.[4] Often, properties are driven by competition between different order parameter fields, for example, the interplay between polarization and structural order parameters gives rise to antiferroelectrics,[5] magnetoelectric coupling in multiferroics,[6] and strain-controlled metal−insulator transitions in VO_2.[7] Remarkably, in all cases, these physical properties can be traced to changes in the symmetry or arrangement of the BO_6 octahedra (cation off-centering, deformation, and tilt system).

Further interest in such behavior has emerged from the fabrication of novel heterointerfaces that allow new functionalities that do not exist in the bulk, including interface superconductivity,[8] improper ferroelectricity,[9] and magnetoelectric coupling phenomena.[10] Even at homophase interfaces, such as ferroelastic domain walls, symmetry changes alone often give rise to new properties, such as recently reported domain wall conductance[11,12] or even superconductivity.[13] Often, these coupling mechanisms show a fascinating interplay with defects that can control order parameter coupling or serve as pinning centers for ferroic domain walls.[14] As demonstrated by the Imry−Ma analysis,[15] materials with

*Address correspondence to albinab@ornl.gov.

Received for review May 24, 2010 and accepted September 20, 2010.

Published online October 4, 2010.
10.1021/nn1011539

domain walls containing significant disorder can span significant volume, consequently imparting interfacial behavior to the bulk.

The key challenge in understanding such emergent functional behaviors in strongly correlated oxides is to probe the coupling mechanisms locally to reveal the interactions between the order parameter fields. Specifically for perovskite materials, the challenge is to link polarization, octahedral tilts, and Jahn−Teller distortions to local atomic and electronic structure and bonding, on a single unit cell level. Recently, direct structural mapping of the polarization field by high-resolution transmission electron microscopy was demonstrated by Jia *et al.*[16,17] and further extended to octahedral tilts.[18] However, the analysis based on geometric calculation of tilts requires simultaneous detection of cation and anion positions, limiting the usable sample thicknesses to values under 10 nm which are difficult to achieve routinely. Additionally, very thin areas can be prone to beam damage and elastic relaxation and/or exhibit significant surface and size effects. These factors significantly complicate interpretation of the results.

Here we introduce a new technique for robust mapping of order parameters in complex oxides and demonstrate mapping of coupled octahedral tilt and polarization dynamics on uncharged and charged domain walls in $BiFeO_3$ (BFO). The method is based on a shape analysis of atomic columns using a high-angle annular dark field (HAADF) image taken with a scanning transmission electron microscope (STEM). Z-contrast images resolve only the heavy atomic columns, while the lighter O neighbors are not distinguishable. We show that the exact column shape contains sufficient information on the positions of the unresolved light atom columns to map octahedral tilt patterns, unit cell by unit cell. We apply the technique to a charged ferroelectric domain wall in a BFO thin film and compare the results with a classical 109° wall. Coupled with geometric measurements of cation displacements, we demonstrate that while the width of the charged domain wall with respect to cation displacements is of the order of several nanometers, in agreement with existing theoretical models,[2,19] the octahedral tilt-related distortions demonstrate an unexpectedly abrupt transition confined to one unit cell. These observations allow us to separate the polarization and structural contributions to the domain wall energy and to predict the behavior of other topological defects in BFO. For the uncharged crystallographically defined 109° wall, the width with respect to cation displacements is about 1.2 nm.

Modeling and Shape Principal Component Analysis (PCA) Analysis. As a model system, we have chosen rhombohedral BFO grown on a conductive $(La_{0.67}Sr_{0.33})MnO_3$ electrode in (100) orientation. In rhombohedral BFO, the interplay between the polarization and the octahedral tilts gives rise to intriguingly complex phase diagrams.[20,21] High-symmetry phases can be metallic,

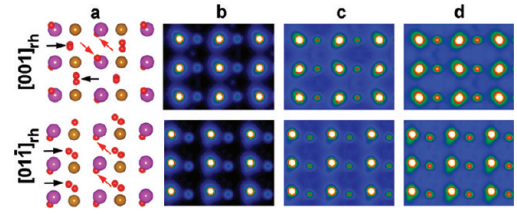

Figure 1. Ball-and-stick models (Bi is purple, Fe is brown, and O is red) (a) and HAADF image simulations for different sample thicknesses at (b) 10, (c) 20, and (d) 30 nm of the two distinct BFO projections corresponding to the ⟨110⟩ pseudocubic direction: $[001]_{rh}$ and $[01\bar{1}]_{rh}$ (top and bottom panels, respectively).

giving rise to a rich spectrum of possible metal−insulator transitions in the bulk and also at interfaces and domain walls.[21] This interplay between structural (octahedral tilts and unit cell tetragonality) and polarization order parameters makes local studies on the level of a single defect or a domain wall or interface particularly important for understanding and controlling materials properties. For the purpose of this work, the multiple ferroelastic states allow us to distinguish different projections of the domains and, hence, explore these effects systematically. BFO offers the advantage of relatively large cation displacements that can be directly visualized by STEM and correlated with octahedral tilt patterns.

To illustrate the feasibility of direct structural analysis of BFO using atomic shapes of the A-site cation columns and establish the possible experimental geometries for these observations, we first perform Bloch wave image simulations[22] with thermal diffuse scattering included using an Einstein model.[23] The $\langle 110\rangle_{pc}$ (pseudocubic) orientation affords the best conditions for the observation of octahedral tilt patterns. In rhombohedral BFO, the parent cubic symmetry is broken, so there are six directions corresponding to the $\langle 110\rangle_{pc}$ direction, but all of these orientations produce only two distinct projections that cannot be related by in-plane symmetry operations: the $[001]_{rh}$ and $[0\bar{1}1]_{rh}$ directions, as shown in Figure 1a. The apparent symmetry of these projections with respect to the oxygen sublattice is notably different: the $[001]_{rh}$ projection shows a checkerboard pattern of oxygen displacements, while in $[0\bar{1}1]_{rh}$ projection all oxygen sites appear identical from cell to cell, resulting in uniform spatial distribution. This holds for oxygen columns that are located between Fe columns, "equatorial" oxygens (denoted by black arrows), as well as those almost overlapping with Bi columns, "axial" oxygens (denoted by red arrows). The simulated HAADF images for different sample thickness in the two orientations are shown in Figure 1b−d. As expected, in the presence of atoms as heavy as Bi, equatorial oxygen columns cannot be seen, except for a faint hint in the image of the thinnest sample. However, at higher thicknesses (20 nm and above; also see Supporting Information) the shape of the Bi column is visibly altered due to the presence of the overlapping axial oxy-

gen columns. Hence, the information on oxygen positions is thus not lost but is rather exhibited in the shape of the A-cation atomic columns. The increased visibility of the axial oxygen columns at higher thicknesses is due to their proximity to the Bi columns, enabling them to recapture some of the intensity scattered from the strongly channeling Bi. This shape distortion follows the same pattern as the oxygen displacements in the structure, a checkerboard pattern for the $[001]_{rh}$ projection and a flat pattern for the $[0\bar{1}1]_{rh}$ projection. Notably, Fe displacements have a uniform spatial distribution in both projections, enabling us to differentiate between the polarization- and tilt-related changes. A similar effect of alteration of the heavy-element column due to adjacent light-element column was observed by Lebeau *et al.*,[24] however the authors considered the resulting change in intensity rather than shape.

To systematically analyze these data and recover information on ordering and oxygen octahedral tilts from images with only cation columns visible, we develop a column-shape analysis procedure based on principal component analysis (PCA) of images. This approach is similar to the method currently used for shape and image recognition in machine vision applications.[25] Briefly, the exact positions of atomic columns are determined using an iterative centroid algorithm, where first a grid of initial guesses is generated and then the "center of mass" is found for each column. This analysis provides the coordinates (x_{ij}, y_{ij}) of the atomic column centers in the *i*-th lattice column and *j*-th row of the square lattice. A square segment of the image 17−21 pixels across (depending on atomic column type) is then selected around each position. Images used for this analysis should have, on one hand, sufficient resolution for quantification of atomic positions (at least 25 pixels/unit cell), and on the other hand, sufficient field of view such that the number of analyzed columns is much larger than the number of PCA components used in the interpretation of the results. Experimental images used in this paper had 34−37 pixels/unit cell.

Subsequently, the set of image segments around the atomic columns is analyzed using principal component decomposition, *i.e.*, each column shape is represented as a linear superposition of orthonormal eigenvectors with position-dependent weight factors:

$$S_{ij} = a_{ij}(k)w_k \qquad (1)$$

where the eigenvectors w_k are orthonormal and a_{ijk} are position-dependent weight coefficients. In traditional PCA, summation is truncated after the first several statistically significant components are chosen based on an eigenvalue criterion.[26] In PCA analysis, details of eigenvector structure and orderings and spatial correlations[27] in the weight coefficient maps provide additional information on the relevance of particular components. Notably, the PCA decomposition (before truncation of the series in eq 1) is a linear operation that preserves the information content of the system[28] and allows representing the data as a sum of uncorrelated components ranked in the order of significance.

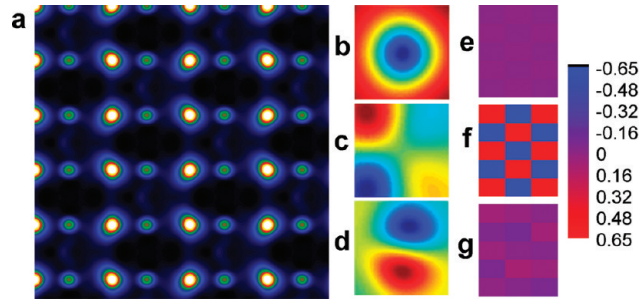

Figure 2. Shape PCA analysis of a simulated ADF image in the $[001]_{rh}$ orientation (a): first three eigenshapes (b−d) and the corresponding weight factor maps (e−g). Color scale is given to the right of the weight factor maps. Fifteen 51 × 51 pixel patches were used for analysis.

For PCA applied to image analysis, the eigenvectors w_k are essentially elementary statistically-independent shapes of atomic columns (eigenshapes), and the $a_{ij}(k)$ are independent maps of the coefficients that quantify the relative contribution (weight) of each shape at the *i,j* lattice site. The eigenshapes and weight coefficient maps for the simulated BFO image in $[001]_{rh}$ orientation are shown in Figure 2. Note that the first two eigenshapes (Figure 2b and c) have clear physical interpretations. The first PCA component (Figure 2b) reflects the average shape of the atomic column, and the corresponding map is almost uniform. Note that the residual checkerboard contrast in (Figure 2e) corresponds to minute (<0.01% of maximum) changes of weight factors and hence is insignificant. The second PCA component (Figure 2c) corresponds to column ellipticity. The corresponding map shows clear checkerboard ordering, with the different checkerboard "sublattices" having opposite signs of weight factors, so the contrast is ~100% from column to column. The third and higher order PCA components are in this case statistically insignificant and are related to finite image size and pixelation effects (*i.e.*, atomic spacing being incommensurate with pixel size).

This simple example clearly illustrates that PCA shape analysis allows us to consistently describe column shape and shows how the corresponding weight factor maps contain information on spatial variability. Very importantly, we note that the presence of spatial correlations (in this case, checkerboard ordering) in the PCA loading maps allows clear differentiation of effects related to intrinsic lattice phenomena (ordered structures) from extrinsic effects, such as drift. This criterion is complementary to the classical eigenvalue approach (scree plot) in PCA and is expected to be particularly important for spatially resolved data.[26] With respect to drift effects, the presence of spatially uni-

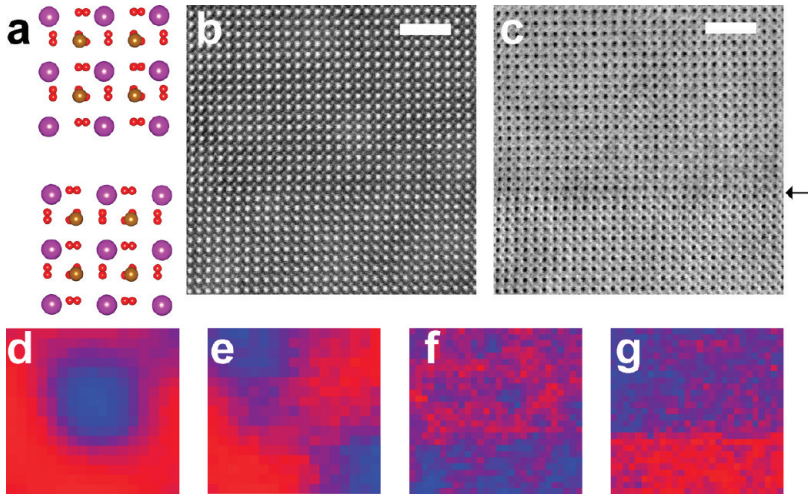

Figure 3. (a) Structure model illustrating changes at the 109° domain wall. Unlike in Figure 1a, Fe displacements and O positions have the same spatial distribution pattern. (b) HAADF and (c) BF STEM images of a 109° domain wall in BFO. Bars are 2 nm. Note: the domain wall is visible in (c) (arrowed) but not in (b). (d and e) First two eigenshapes and (f and g) corresponding weight factor maps for Fe column shapes. The weight factor map for the second eigenshape, the diagonal displacement, shows clear domain wall contrast. Images (d−g) are shown in color scale normalized from minimum to maximum for each. For analysis, 756 17 × 17 patches were used. There is a small lateral translation evident in the vicinity of the domain wall, possibly caused by sample charging.

form drift is exhibited as a change in the first PCA eigenshape, any random line-to-line noise generally filters out with the statistically insignificant components, and only the drift gradient across the image appears in the second, third, and higher statistically significant PCA eigenshapes. This remarkable property of PCA transform is highly reminiscent of recent analyses of SPM data, where the instrumental drifts were observed to be selected in a limited number of PCA components.[27,29] In the next section, we apply this approach to the analysis of experimental data.

Domain Wall Imaging in BFO. Studies of domain wall structure in BFO grown on (001) substrates and associated changes in polarization and octahedral tilts present a dilemma concerning the choice of appropriate observation conditions. The crystallographically permissible 71° (oriented in $(110)_{pc}$ planes at 45° to growth direction) and 109° (oriented in $(100)_{pc}$ planes) walls are best observed down a $[100]_{pc}$ zone axis as this orientation is required for "edge-on" wall alignment. However, in $[100]_{pc}$ projection, cation displacements and oxygen positions have the same spatial distribution pattern (Figure 3a) and thus cannot be examined separately using the proposed technique. In this case the shape PCA analysis is expected to provide information on the dominant distortion, *i.e.*, polarization. Experimental HAADF and BF images of a 109° domain wall are given in Figure 3b and c, respectively. The PCA eigenshapes and weight factor maps obtained by analysis of Figure 3b for Fe columns are shown in Figure 3d−g, respectively. The first PCA component represents the average atomic column shapes and shows small spatial variation (10% of maximum), likely due to intensity changes because of a small difference in the orientation of the two domains with respect to the beam direction. The third, fourth, and higher components are dominated by noise, and the corresponding weight factor maps are essentially featureless. In comparison, the weight factor map for the second PCA component clearly shows the localization of the domain wall (Figure 3g) as well as 100% contrast. The second eigenshape corresponds to the diagonal distortion of the cation column periphery, in this case caused by proximity of the more intense Bi column. For different polarization orientations, the closest Bi column is located on the opposite sides of the unit cell diagonal in the image plane (Figure 3e). Note that the wall is invisible on the dark-field image *per se* (but is visible on the bright-field image) and can be revealed only by PCA or atomic displacement analysis. Shape analysis of the Bi columns did not reveal any components with changes localized at the domain wall.

While observing the crystallographically allowed domain walls down the $[100]_{pc}$ zone axis does not allow decoupling of polarization and tilt effects, these constraints do not apply to nonequilibrium domain walls. Similar to many other perovskite materials, in the thin foil-type geometries used for TEM studies, the domain walls can strongly deviate from classical orientation to minimize the wall energy due to depolarization forces (which favor alignment in the thinnest, *i.e.*, beam direction). Charged domain walls can also be moved by external stimuli away from their equilibrium orientation, enabling other possible configurations, including some which will be edge-on for the $[110]_{pc}$ observation direction. In the following sections we examine the structural behavior around one such charged wall.

Simultaneously acquired bright- and dark-field images of the vicinity of a domain wall in BFO are shown in Figure 4a and b. From the geometry of experimental observations, the wall is identified as a $(1\bar{1}1)_{pc}$ charged wall between $[111]_{pc}$ and $[1\bar{1}\bar{1}]_{pc}$ polarization states. In this attribution we assumed that the observability and the sharpness of the contrast imply that the wall is close to edge-on orientation with respect to the beam. The results of the PCA analysis of the HAADF image in Figure 4a are shown in Figure 4c−h. The first PCA eigenshape again represents the average shape of the atomic column and corresponds to an almost spatially uniform weight factor map, where the signal change across the interface is small and reflects a slight difference in domain orientation. However, the second and third PCA weight factor maps illustrate a very abrupt transition

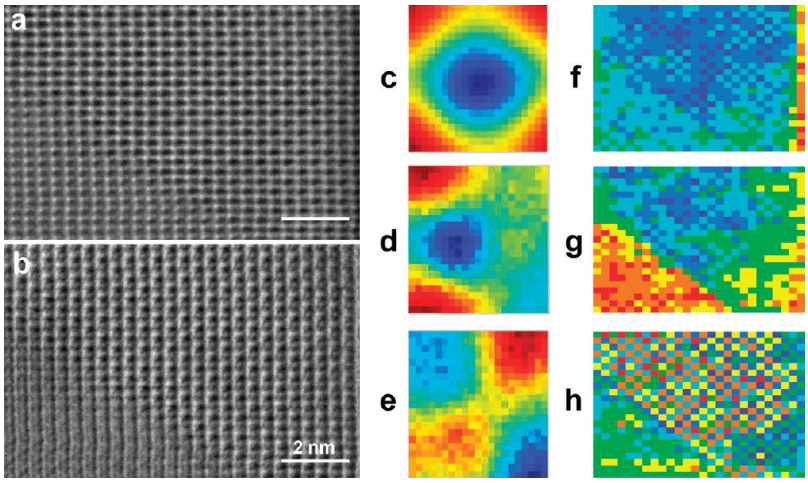

Figure 4. Shape PCA analysis of experimental data: (a) HAADF image used for analysis, (b) simultaneously acquired BF image showing domain contrast, (c−e) first three eigenshapes, and (f−h) corresponding weight factor maps. Note that, unlike for the 109° wall, there are three above-noise PCA components with distinct spatial distribution of weight factors. For analysis, 598 21 × 21 patches were used.

across the domain wall. Notably, the second PCA eigenshape (Figure 4d, off-center widening) shows a steplike contrast across the domain wall (Figure 4 g) and hence is likely related to the changes in the unit cell shape across the interface. Note that we expect a larger number of statistically significant eigenshapes for PCA here than for modeling, since we have two possible domain orientations and multiple experimental effects.

The most interesting behavior is observed in the weight factor map for the third PCA eigenshape (Figure 4h), which is essentially zero in the lower left domain and forms a checkerboard ordering in the upper right domain. Comparison with the modeling results as well as symmetry considerations thus indicates that the third eigenshape (Figure 4e, diagonal extension similar to Figure 2c) is related to the diagonal column distortion and thus octahedral tilts. Thus, we see that this approach allows direct mapping of octahedral tilts, with the intensity of the respective PCA component being related to tilt angle. This attribution (as opposed to octahedral deformation in the vicinity of the wall for example) is confirmed by the saturation of the loading maps away from the wall, *i.e.*, in the regions with bulk structure. Moreover, in this case we can identify the upper right domain as $[001]_{rh}$-type projection with a checkerboard order of tilts, while the lower left domain appears to be a $[0\bar{1}1]_{rh}$-type projection with a uniform spatial distribution of tilts.

To further illustrate this statement, Figure 5 shows close-ups of several atomic column images. In panel A, we can see two Bi atom columns taken from different checkerboard sublattices from the upper right domain. The elliptical character and opposite tilts of the ellipses are clearly seen. The bottom panel shows atomic column shapes reconstructed from the first three eigenshapes. Both the elliptical character and the opposite nature of the tilts are captured in the reconstructions, demonstrating that three components provide an adequate description of the atomic shapes along with a remarkable reduction in noise. In panel B, close-ups of the two Bi atoms from the lower left domain are given. The shapes of these atoms are clearly different from those in A; they have no apparent ellipticity (although they do have a different shape distortion) and are similar to each other. The same features are reflected in the three-component reconstruction (bottom row).

Changes Across the Domain Wall and Comparison with Ferroelectric Displacements. To quantify polarization and tilt behavior across the domain walls, we systematically analyze the PCA weight factor maps as well as the cation displacement maps calculated from the same images. For the case of a charged domain wall, the two phenomena can be efficiently decoupled from each other by PCA, since they are manifested at different spatial frequencies. PCA clearly illustrates an abrupt change in characteristic column shape across the interface, as seen in Figure 4. In Figure 6a we show the map of the absolute values of the weight factors for the third eigenshape describing column ellipticity, to show the magnitude of ellipticity but not the sign. The map also shows abrupt contrast at the domain wall. If we gener-

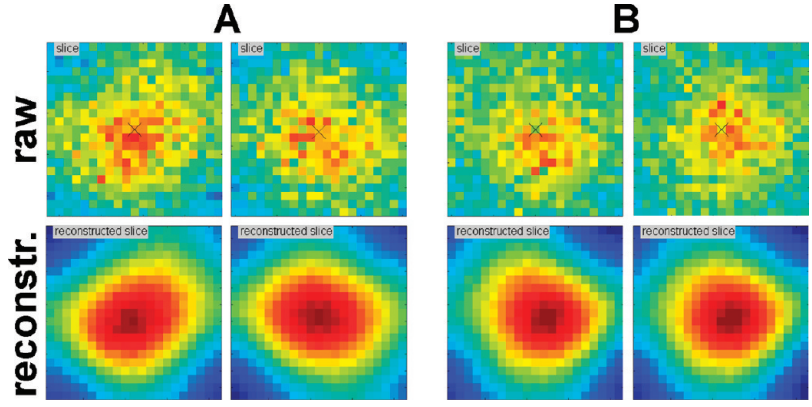

Figure 5. Raw (top) and reconstructed (bottom) image slices taken from the image in Figure 4a. Panel A shows two atomic columns from the upper right domain located on different checkerboard sublattices; their elliptical character and different "tilt" angles are apparent. Panel B shows two atomic columns from the bottom left domain; columns here are all similar in shape to each other but different from those in A.

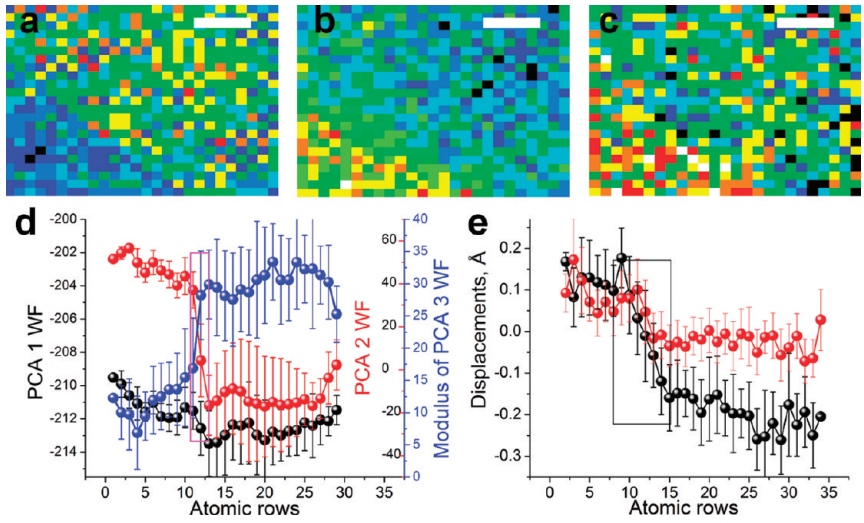

Figure 6. Comparison of the spatial variation of the column shapes and the ferroelectric polarization across the domain wall: (a) absolute value of the third PCA weight factor map (see Figure 4h). (b and c) Polarization maps for out-of-plane (b) and in-plane (c) polarization based on the Bi and Fe column displacements measured from the Z-contrast image. (d) Profiles of different PCA weight factor maps across the domain wall: first (black) (see Figure 4f), second (red) (see Figure 4g), and the absolute value of the third component (blue) (see Figure 6a); note the atomically sharp transition in the second and third PCA weight factor map profiles. (e) Profiles of out-of-plane (black) and in-plane (red) polarization maps (see b and c) across the domain wall showing a diffuse transition. Scale bars are 2 nm.

ate a profile of this map by averaging perpendicular to the wall direction, we see that this contrast is indeed atomically abrupt (Figure 6d, blue curve). The profile of the second PCA weight factor map also shows an abrupt change (Figure 6d, red curve), suggesting that the predominant shape distortion switches from elliptical checkerboard to off-center widening across the domain wall. No apparent change is observed in the profile of the weight factor map for the first eigenshape representing the average column shape, as given by the black curve in Figure 6d.

To complement this data, we analyze the behavior of atomic displacements of Fe columns across the domain wall, which are related to ferroelectric polarization. To determine Fe displacements, we use a direct measurement of the atomic column positions of Bi and Fe from a Z-contrast image, as described elsewhere.[30] The spatial maps of the displacement components perpendicular to the interface (Figure 6b) and along the interface (Figure 6c) have a considerably wider transition associated with the domain wall. The corresponding profiles (Figure 6e) clearly show that the width of the domain wall with respect to cation displacements is 6−7 unit cells.

Similar analysis can be performed for the image of the equilibrium domain wall in Figure 3b. Figure 7a and b shows color maps of the Fe displacements in *x* (along the wall) and *y* (normal to the wall) directions, respectively. Sharp change is seen in Figure 7a but not in b, in agreement with the expected behavior of polarization components across ferroelectric wall (no discontinuity of normal polarization component). This is further illustrated by the displacement profiles (Figure 3c) generated from Figure 7a and b by averaging over the *x* coordinate. The transition width for *x* displacement is ~3 unit cells, or about 1.2 nm. In comparison, the second PCA weight factor map generated by shape analysis of the Fe columns (Figure 3i) shows the same transition width, as illustrated by the profile in Figure 7d, confirming our assumption that polarization is the dominant contribution to shape distortion for this sample orientation.

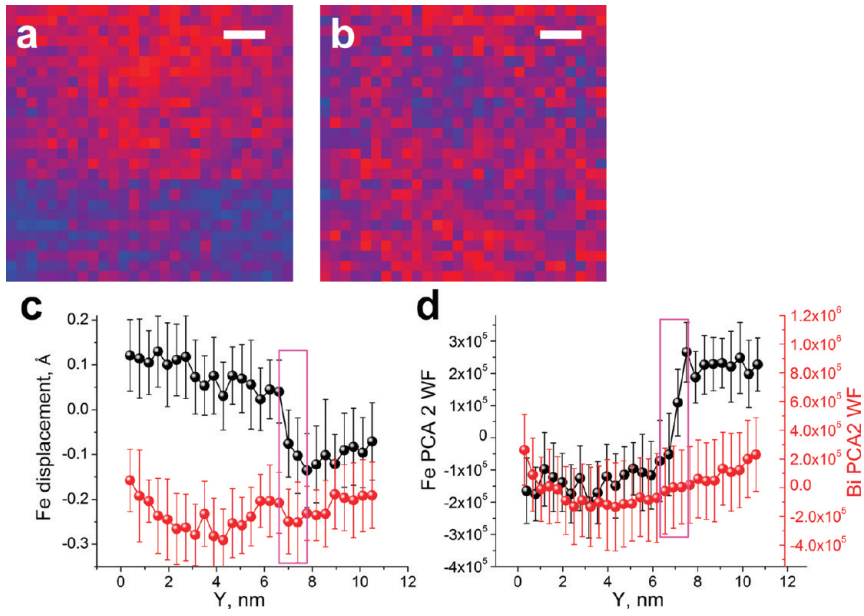

Figure 7. Comparison of the spatial variation of the column shapes and ferroelectric polarization across the domain wall for the image in Figure 3b: (a and b) Fe displacement components along (a) and normal (b) to the domain wall based on the Bi and Fe column positions; each point represents one unit cell. Domain wall is evident in (a). (c) Profiles of (a) (black) and (b) (red) across the domain wall, showing a transition of ~3 unit cells wide [for (a)]. (d) Profiles of second PCA weight factor maps of Fe (black) and Bi (red) across the domain wall, also showing a transition of ~3 unit cells wide (for Fe). Scale bars are 2 nm.

To interpret these observations, we recall the recent studies of domain wall behavior in BFO. For uncharged domain walls, the behavior of the polarization and the octahedral tilts was analyzed in depth by Spaldin *et al.*[31] They have demon-

strated that: (i) in all cases the polarization profile across the wall is relatively narrow (of the order of 1−2 unit cells) and (ii) the walls with continuous octahedral tilts have much lower energy. In this discussion, we note that while octahedral tilts and polarization instability are coupled in BFO, they are driven by instabilities originating in different regions of the Brillouin zone, namely zone center *G* for polarization and *R* for the octahedral tilts. While the exact high-temperature phase diagram for BFO is controversial, the accepted sequence of phase transformations include $Pm\bar{3}m$ to *Pbnm* transition at 1204 K and subsequently *Pbnm* to *R*3*c* at 1098 K. In the *R*3*c* phase, the antiphase walls corresponding to the discontinuity of the tilt order parameter will have the same $(100)_{pc}$ and $(110)_{pc}$ orientations as the ferroelectric domain walls. Hence, antiphase and ferroelectric boundaries can either coincide or exist separately. The analysis of Spaldin *et al*. provides the energies for a pure ferroelectric wall and a ferroelectric−antiphase boundary wall, respectively (albeit not for a pure antiphase boundary).

Ginzburg−Landau Analysis of Wall Behavior. Using the measured profiles for polarization- and tilt-related (antiferrodistortive) order parameters, the contributions of these order parameters to the total energy of the domain wall can be estimated. For a ferroelectric with a first-order transition the free energy density is

$$f(P, E) = \frac{\alpha(T)}{2}P_3^2 + \frac{\beta}{4}P_3^4 + \frac{\gamma}{6}P_3^6 - P_3E \qquad (2)$$

where $\alpha(T) = a(T - T_c)$ is the temperature dependent coefficient, and T_c is the corresponding Curie temperature. For systems with several competing interactions (*e.g.*, antiferroelectrics or ferroelectrics with structural instabilities), the free energy is represented as $f = f_P + f_\chi + f_{P\chi}$, where f_P and f_χ are power expansions similar to eq 4 with respect to polarization, *P*, and structural, χ, order parameters, and the coupling term $f_{P\chi}$ is typically taken as the lowest symmetry allowed combination, *e.g.*, $f_{P\chi} = P^2\chi^2$. The phase diagram for such materials has been studied by Tagantsev and Balashova.[5] We can define two characteristic coefficients for the two order parameters: $a_1(T) = a_{1T}(T - T_c)$, where T_c is the Curie temperature of paraelectric−ferroelectric phase transition, and $b_1 = b_{T1}(T - T_S)$, where T_S is the temperature of the structural phase transition. The dynamic of systems characterized by vector polarization and structural order parameters has been extensively developed by Haun and Cross for the PZT solid solutions.[32,33] The theory of domain walls in the systems with vector polarization order parameters has been recently analyzed by Hlinka.[19,34] The dynamics and order parameter profiles of domain walls in the system with two scalar order parameters were analyzed by Sonin and Tagantsev.[35]

Neglecting the electrostriction, the wall energy can be approximated as $\psi_P \approx 16L_PP_S^2|a_1|^3/3$, where L_p is domain wall width, P_s is saturation polarization, and a_1 is the characteristic coefficient defined above (see Appendix I for full derivation). The estimates for the BFO materials parameters yield saturation polarization of $P_S = 89\ \mu C/cm^2$ (as compared to 90 $\mu C/cm^2$ calculated by Spaldin *et al*.).[31] The wall width is estimated from the experimental data as 1.4 atomic rows, and effective lattice constant is 0.55 nm, and allows evaluating the wall energy. With electrostriction, the effective gradient term is $g = 7.5 \times 10^{-10}$ m^3/F, and the wall energy is $\psi_P = 956\ mJ/m^2$. Without electrostriction, $q = 0$ and $g = 5.4 \times 10^{-10}\ m^3/F$, and the wall energy is $\psi_P = 687\ mJ/m^2$. These numbers compare favorably to the estimates by Spaldin *et al*.[31] of $\psi = 829\ mJ/m^2$ for 180° domain wall.

Corresponding tilt wall energy is $\psi_S \approx 16L_S\theta_S^2|b_1|^3/3$, where L_S is the wall width with respect to tilts, θ_S is the saturation value of the tilt, and b_1 is the characteristic coefficient for the structural phase transition defined above. L_S is estimated from the experimental halfwidth as 0.5 atomic rows, and the effective lattice constant is 0.55 nm. Hence, the structural contribution to the wall energy is $\psi_S = 118-170\ mJ/m^2$. Based on these estimates, the structural contribution to the ferroelectric wall energy is relatively small, of the order of 10−20%, and the structural wall is narrow. Notably, analysis by Spaldin *et al*.[31] suggests that for the antiphase walls with discontinuous octahedral rotations, the wall energies are significantly higher (*e.g.*, 896 vs 205 mJ/m^2 for 109° wall). Given that material parameters are universal, this analysis suggests that such antiphase walls will be very broad, of the order of 5−10 atomic rows.

SUMMARY

A new sensitive method of analyzing structural distortions including octahedral tilts and polarization in functional perovskites based on column shape is introduced. Applying principal component analysis (PCA) to cation column shapes in high-angle annular dark field (HAADF) images reveals the orientation of a domain wall and the surrounding domains from just one image. It provides a measure of the octahedral tilts without the need to visualize oxygen atoms directly thus allowing octahedral tilt analysis in considerably thicker samples, minimizing beam damage and improving statistics. For crystallographically allowed 109° domain wall, the overall width is 1−2 u.c. For charged walls, the shape PCA approach allows polarization and tilt effects to be decoupled. Intriguingly, the wall is very thin in images of octahedral rotation, while relatively wide with respect to polarization. Using the experimentally measured structural and polarization domain wall thickness as input for the Ginzburg−Landau type theory, we can estimate the polarization and the structural contributions to the wall energy. It is shown that for the wall with continuous octahedral rotations, the wall energy is dominated by polarization (80−90%), with only minor contribution from structural order parameter.

In many systems, notably in perovskites, structural distortions are of a paramount importance due to their direct influence on properties. In many complex oxide

systems tilts of the oxygen octahedra probably lie at the heart of many of the remarkable interfacial properties so far reported. The suppression or induction of octahedral tilts across interfaces can transform insulators into metals or *vice versa* and induce new magnetic or ferroelectric states. The quantitative shape PCA approach to extract subresolution information from images of distorted structures offers new possibilities to map these minute but critical structural details unit cell by unit cell. Using these measurements, contributions to domain wall energy from different order parameters can be estimated. The details of quantification of the results.

METHODS

Materials. $BiFeO_3-La_{0.7}Sr_{0.3}MnO_3$ (BFO−LSMO) heterostructures were fabricated by pulsed-laser deposition with reflection high-energy electron diffraction (RHEED) control of growth process. Atomically smooth TiO_2-terminated $SrTiO_3$ (STO) (100) substrates were prepared by a combined HF-etching/annealing treatment. All substrates had vicinal angles of ~0.1°. Stoichiometric LSMO, SRO, and BFO targets were ablated at a laser fluence of ~1.5 J cm^{-2} and a repetition rate of 1 or 2 Hz for the growth of LSMO and BFO, respectively. During growth, the substrate was held at 750 °C, in an oxygen environment at 200 mTorr for LSMO,[36] while for BFO the conditions were adjusted to 670 °C and 100 mTorr.[37] RHEED analysis demonstrated intensity oscillations indicating a layer-by-layer growth mode without any island formation. After the growth, the heterostructures were slowly cooled to room temperature in 1 atm of oxygen at a rate of ~5 °C/min to optimize the oxidation level.

STEM and Image Simulations. Cross-sectional samples for STEM analysis were prepared by mechanical thinning, precision polishing, and ion milling. The STEM data was acquired using a VG microscopes HB603U operated at 300 kV and equipped with a Nion aberration corrector. ADF image simulations were carried out using Bloch wave code[22] including absorption due to thermal diffuse scattering. A probe forming aperture semiangle of 23 mrad was used in all cases, and an ADF detector inner angle of 65 mrad was assumed. Coherent aberrations typical of the aberration corrected VG HB603U were used, with a defocus of 20 Å with third- and fifth-order spherical aberrations of −0.037 and 100 mm, respectively.

PCA Analysis. The eigenshapes w_k and the corresponding eigenvalues λ_k are found from the covariance matrix, $\mathbf{C} = \mathbf{A}\mathbf{A}^T$, where $\mathbf{A}$ is the matrix of all experimental data points $\mathbf{A} = S_{lm}$, *i.e.*, the rows of $\mathbf{A}$ correspond to individual grid points ($l = 1, ..., i \cdot j$), and the columns correspond to points in shape section, $m = 1, ..., P^2$, where P is the number of pixels in image segments. The eigenshapes w_k are orthogonal and are chosen such that corresponding eigenvalues are placed in descending order, $\lambda_1 > \lambda_2 >$, *etc*. The eigenvalues and eigenshapes are determined through singular value decomposition of the $\mathbf{A}$ matrix.

Material Parameters for BFO Collected from Refs 21 and 38. Here we use the following GLD parameters for BFO: $a_{1T} = 4.9 \times 10^5$ m/(F K), $T_c = 1098$ K, $T = 300$ K, $a_{11} = 6.5 \times 10^8$ $m^5/(C^2F)$, $a_{12} = 1.0 \times 10^8$ $m^5/(C^2F)$, $Q_{11} = 0.032$ m^4/C^2, $Q_{12} = -0.016$ m^4/C^2, $Q_{44} = 0.01$ m^4/C^2, $s_{11} = 5.29 \times 10^{-12}$ m^2/N, $s_{12} = -1.85 \times 10^{-12}$ m^2/N, and $s_{44} = 1.47 \times 10^{-12}$ m^2/N. For structural order parameter, $\theta_S = 11-12^c$, $T_S = 1204$ K, $c_{11} = 3.02 \times 10^{11}$ N/m^2, $c_{12} = 1.62 \times 10^{11}$ N/m^2, $c_{44} = 0.68 \times 10^{11}$ N/m^2, $a_{hex} = 5.58$ A, and $c_{hex} = 13.90$ A.

Acknowledgment. This research was sponsored by the Division of Materials Sciences and Engineering, Office of Basic Energy Sciences of the United States Department of Energy (A.B., H.J.C., S.J.P., and S.V.K.). O.O. was supported by ORNL HERE program. The authors also acknowledge invaluable advice from Dr. Alexander Tselev (UT and ORNL) and helpful discussions with Prof. Ekhard Salje (Cambridge University).

Supporting Information Available: Thickness dependence of the diagonal distortion of the column shapes analyzed by PCA. This material is available free of charge *via* the Internet at http://pubs.acs.org.

APPENDIX I

We analyze the domain wall energy using an approximate bulk free energy functional corresponding to ideal cubic perovskite symmetry of the polar and structural order parameters:

$$G_b = \left(\begin{array}{l} \frac{a_1}{2}(P_1^2 + P_2^2 + P_3^2) + \frac{a_{12}}{2}(P_1^2P_2^2 + P_1^2P_3^2 + P_3^2P_2^2) + \\ \frac{a_{11}}{4}P_1^4 + \frac{a_{33}}{4}(P_2^4 + P_3^4) + \frac{a_{111}}{6}(P_1^6 + P_2^6 + P_3^6) + \\ \frac{a_{123}}{2}P_3^2P_2^2P_1^2 + \frac{a_{112}}{4}(P_3^4(P_1^2 + P_2^2) + P_1^4(P_2^2 + P_3^2) + \\ P_2^4(P_1^2 + P_3^2)) + \frac{1}{2}g_{ij}(\nabla P_i \nabla P_j) + \frac{b_i}{2}\theta_i^2 + \frac{b_{ij}}{4}\theta_i^2\theta_j^2 + \\ \frac{b_{ijk}}{6}\theta_i^2\theta_j^2\theta_k^2 + \frac{\eta_{ij}}{2}\theta_j^2P_i^2 + \frac{v_{ij}}{2}(\nabla\theta_i\nabla\theta_j) \end{array} \right) \quad (3)$$

Voight notations are used, ∇ is the gradient operator, crystallographic axes are 1, 2, and 3. Gradient coefficients g_{ij} and v_{ij} are regarded positive for commensurate ferroics, and θ_i are the structural order parameter components (*e.g.*, octahedral tilt angles). In the absence of coupling, the eq 3 would describe first-order ferroelectric and ferroelastic, respectively. The coupling constants between θ_i and polarization components P_i are defined by η_{ij}.[32,33]

In decoupling 1D approximation the polarization profile across the uncharged 180° domain wall in the energetically preferable at room temperature rhombohedral phase ($P_1 = P_2 = P_3$, x is perpendicular to the wall and belongs to the plane [111]) can be approximated as

$$P(x) = P_S \cdot \tanh((x - x_0)/2L_p) \quad (4)$$

The polarization far from the wall, P_S, wall width, L_p, and domain wall energy ψ_P are respectively

$$P_S = \sqrt{\frac{-3a_1}{2(a_{11} + a_{12})}}, \qquad L_P = \sqrt{\frac{g}{-2a_1}}\left(1 + \frac{3q}{2(a_{11} + a_{12})}\right)^{-1/2} \quad (5)$$

$$\psi_P = \sqrt{g\left(1 + \frac{3q}{2(a_{11} + a_{12})}\right)}\frac{(-2a_1)^{3/2}}{a_{11} + a_{12}} \quad (6)$$

where effective gradient term is $g = g_{11} + g_{12}$, parameter $q = ((Q_{11}^2 + Q_{12}^2)s_{11} - 2Q_{11}Q_{12}s_{12})/(s_{11}^2 - s_{12}^2)$ is the renormalization due to electrostrictive coupling at the wall (Q_{ij} are the electrostriction tensor components, s_{ij} are elastic compliances).

Similarly to polarization, the scalar octahedral tilt profile of the alternating "sublattices" with the same signs of tilts can be approximated as

$$\theta(x) = \theta_S \cdot \tanh((x - x_0)/2L_S) \quad (7)$$

where $L_S = \sqrt{v/2|b_1|}$, $\theta_S = \sqrt{-b_1/b_{11}}$ and is about 11−12°.

To determine parameter b_1 for BFO, we utilize the relation between the cell deformation and the tilt angle as $\cos\delta = (4 - \cos^2\theta_S)/(4 + 2\cos^2\theta_S)$ for rhombohedral perovskites.[39,40] At temperatures higher than T_c but lower than T_S, the unit cell hexagonal parameter ratio is $u_h(\theta_S) = 2.25\sin^{-2}(\delta/2) - 3$. Thus the elas-

tic energy related with the tilt wall can be estimated as $\psi_S \cong c_{11}(u_h(\theta_S)/6 - 1)^2 L_S$, since $u_h(0) = 6$.

REFERENCES AND NOTES

1. Mitchell, R. G. *Perovskites-Modern and Ancient.*: Almaz Press: Thunder Bay, Ontario, 2002.
2. Lines, M.; Glass, A. *Principles and Applications of Ferroelectrics and Related Materials*. Clarendon Press: Oxford, 1979.
3. Dagotto, E. *Phase Separation and Colossal Magnetoresistance*. Springer: New York, 2003.
4. Glazer, A. M. Classification of Tilted Octahedra in Perovskites. *Acta Crystallogr., Sect. B: Struct. Sci.* **1972**, *B 28*, 3384–3392.
5. Balashova, E. V.; Tagantsev, A. K. Polarization Response of Crystals with Structural and Ferroelectric Instabilities. *Phys. Rev. B: Condens. Matter Mater. Phys.* **1993**, *48*, 9979–9986.
6. Fiebig, M. Revival of the Magnetoelectric Effect. *J. Phys. D: Appl. Phys.* **2005**, *38*, R123–R152.
7. Wei, J.; Wang, Z. H.; Chen, W.; Cobden, D. H. New Aspects of the Metal-Insulator Transition in Single-Domain Vanadium Dioxide Nanobeams. *Nat. Nanotechnol.* **2009**, *4*, 420–424.
8. Ohtomo, A.; Hwang, H. Y. A High-Mobility Electron Gas at the $LaAlO_3/SrTiO_3$ Heterointerface. *Nature* **2004**, *427*, 423–426.
9. Bousquet, E.; Dawber, M.; Stucki, N.; Lichtensteiger, C.; Hermet, P.; Gariglio, S.; Triscone, J. M.; Ghosez, P. Improper Ferroelectricity in Perovskite Oxide Artificial Superlattices. *Nature* **2008**, *452*, 732–736.
10. Brinkman, A.; Huijben, M.; Van Zalk, M.; Huijben, J.; Zeitler, U.; Maan, J. C.; Van der Wiel, W. G.; Rijnders, G.; Blank, D. H. A.; Hilgenkamp, H. Magnetic Effects at the Interface between Non-Magnetic Oxides. *Nat. Mater.* **2007**, *6*, 493–496.
11. Seidel, J.; Martin, L. W.; He, Q.; Zhan, Q.; Chu, Y. H.; Rother, A.; Hawkridge, M. E.; Maksymovych, P.; Yu, P.; Gajek, M.; et al. Conduction at Domain Walls in Oxide Multiferroics. *Nat. Mater.* **2009**, *8*, 229–234.
12. Kim, Y.; Alexe, M.; Salje, E. Nanoscale Properties of Thin Twin Walls and Surface Layers in Piezoelectric WO_{3-x}. *Appl. Phys. Lett.* **2010**, *96*, 032904.
13. Aird, A.; Salje, E. Sheet Superconductivity in Twin Walls: Experimental Evidence of WO_{3-x}. *J. Phys.: Condens. Matter* **1998**, *10*, L377–L380.
14. Lee, W.; Salje, E.; Bismayer, U. Influence of Point Defects on the Distribution of Twin Wall Widths. *Phys. Rev. B: Condens. Matter Mater. Phys.* **2005**, *72*, 104116.
15. Imry, Y.; Ma, S. Random-Field Instability of Ordered State of Continuous Symmetry. *Phys. Rev. Lett.* **1975**, *35*, 1399–1401.
16. Jia, C. L.; Mi, S. B.; Urban, K.; Vrejoiu, I.; Alexe, M.; Hesse, D. Atomic-Scale Study of Electric Dipoles near Charged and Uncharged Domain Walls in Ferroelectric Films. *Nat. Mater.* **2008**, *7*, 57–61.
17. Jia, C. L.; Nagarajan, V.; He, J. Q.; Houben, L.; Zhao, T.; Ramesh, R.; Urban, K.; Waser, R. Unit-Cell Scale Mapping of Ferroelectricity and Tetragonality in Epitaxial Ultrathin Ferroelectric Films. *Nat. Mater.* **2007**, *6*, 64–69.
18. Jia, C. L.; Mi, S. B.; Faley, M.; Poppe, U.; Schubert, J.; Urban, K. Oxygen Octahedron Reconstruction in the $SrTiO_3/LaAlO_3$ Heterointerfaces Investigated Using Aberration-Corrected Ultrahigh-Resolution Transmission Electron Microscopy. *Phys. Rev. B: Condens. Matter Mater. Phys.* **2009**, *79*, 081405.
19. Marton, P.; Rychetsky, I.; Hlinka, J. Domain Walls of Ferroelectric $BaTiO_3$ within the Ginzburg-Landau-Devonshire Phenomenological Model. *Phys. Rev. B: Condens. Matter Mater. Phys.* **2010**, *81*, 144125.
20. Lisenkov, S.; Rahmedov, D.; Bellaiche, L. Electric-Field-Induced Paths in Multiferroic $BiFeO_3$ from Atomistic Simulations. *Phys. Rev. Lett.* **2009**, *103*, 047204.
21. Catalan, G.; Scott, J. F. Physics and Applications of Bismuth Ferrite. *Adv. Mater.* **2009**, *21*, 2463–2485.
22. Allen, L. J.; Findlay, S. D.; Oxley, M. P.; Rossouw, C. J. Lattice-Resolution Contrast from a Focused Coherent Electron Probe. Part I. *Ultramicroscopy* **2003**, *96*, 47–63.
23. Allen, L. J.; Rossouw, C. J. Absorptive Potentials Due to Ionization and Thermal Diffuse-Scattering by Fast Electrons in Crystals. *Phys. Rev. B: Condens. Matter Mater. Phys.* **1990**, *42*, 11644–11654.
24. LeBeau, J. M.; Findlay, S. D.; Wang, X.; Jacobson, A. J.; Allen, L. J.; Stemmer, S. High-Angle Scattering of Fast Electrons from Crystals Containing Heavy Elements: Simulation and Experiment. *Phys. Rev. B: Condens. Matter Mater. Phys.* **2009**, *79*, 214110.
25. Haykin, S. S. *Neural Networks and Learning Machines*; 3rd ed.; Prentice Hall: Upper Saddle River, NJ, 2008.
26. Jolliffe, I. T. *Principal Component Analysis*; Springer: New York, 2002.
27. Jesse, S.; Kalinin, S. V. Principal Component and Spatial Correlation Analysis of Spectroscopic-Imaging Data in Scanning Probe Microscopy. *Nanotechnology* **2009**, *20*, 085714.
28. Hyuvarinen, A.; Karhunen, J.; Oja, E. *Independent Component Analysis*. Wiley: Hoboken, NJ , 2001.
29. Nikiforov, M. P.; Reukov, V. V.; Thompson, G. L.; Vertegel, A. A.; Guo, S.; Kalinin, S. V.; Jesse, S. Functional Recognition Imaging Using Artificial Neural Networks: Applications to Rapid Cellular Identification Via Broadband Electromechanical Response. *Nanotechnology* **2009**, *20*, 405708.
30. Borisevich, A. Y.; Chang, H. J.; Huijben, M.; Oxley, M. P.; Okamoto, S.; Niranjan, M. K.; Burton, J. D.; Tsymbal, E. Y.; Chu, Y. H.; Yu, P.; et al. Suppression of Octahedral Tilts and Associated Changes in Electronic Properties at Epitaxial Oxide Heterostructure Interfaces. *Phys. Rev. Lett.* **2010**, *105*, 087204.
31. Lubk, A.; Gemming, S.; Spaldin, N. A. First-Principles Study of Ferroelectric Domain Walls in Multiferroic Bismuth Ferrite. *Phys. Rev. B: Condens. Matter Mater. Phys.* **2009**, *80*, 104110.
32. Haun, M. J.; Furman, E.; Halemane, T. R.; Cross, L. E. Thermodynamic Theory of the Lead Zirconate-Titanate Solid-Solution System, 0.4. Tilting of the Oxygen Octahedra. *Ferroelectrics* **1989**, *99*, 55–62.
33. Haun, M. J.; Furman, E.; Jang, S. J.; Cross, L. E. Thermodynamic Theory of the Lead Zirconate-Titanate Solid-Solution System, 0.1. Phenomenology. *Ferroelectrics* **1989**, *99*, 13–25.
34. Hlinka, J.; Marton, P. Phenomenological Model of a 90 Degrees Domain Wall in $BaTiO_3$-Type Ferroelectrics. *Phys. Rev. B: Condens. Matter Mater. Phys.* **2006**, *74*, 104104.
35. Sonin, E. B.; Tagantsev, A. K. Structure and Phase-Transitions in Antiphase Boundaries of Improper Ferroelectrics. *Ferroelectrics* **1989**, *98*, 291–295.
36. Huijben, M.; Martin, L. W.; Chu, Y. H.; Holcomb, M. B.; Yu, P.; Rijnders, G.; Blank, D. H. A.; Ramesh, R. Critical Thickness and Orbital Ordering in Ultrathin $La_{0.7}Sr_{0.3}MnO_3$ Films. *Phys. Rev. B: Condens. Matter Mater. Phys.* **2008**, *78*, 094413.
37. Martin, L. W.; Chu, Y. H.; Holcomb, M. B.; Huijben, M.; Yu, P.; Han, S. J.; Lee, D.; Wang, S. X.; Ramesh, R. Nanoscale Control of Exchange Bias with $BiFeO_3$ Thin Films. *Nano Lett.* **2008**, *8*, 2050–2055.
38. Zhang, J. X.; Li, Y. L.; Wang, Y.; Liu, Z. K.; Chen, L. Q.; Chu, Y. H.; Zavaliche, F.; Ramesh, R. Effect of Substrate-Induced Strains on the Spontaneous Polarization of Epitaxial $BiFeO_3$ Thin Films. *J. Appl. Phys.* **2007**, *101*, 114105.
39. Megaw, H. D.; Darlington, C. N. W. Geometrical and Structural Relations in Rhombohedral Perovskites. *Acta Crystallogr., Sect. A: Cryst. Phys., Diffr., Theor. Gen. Crystallogr.* **1975**, *A 31*, 161–173.
40. Moreau, J. M.; Michel, C.; Gerson, R.; James, W. J. Ferroelectric $BiFeO_3$ X-Ray and Neutron Diffraction Study. *J. Phys. Chem. Solids* **1971**, *32*, 1315–1320.